◇Review Article◇

Elastography: Imaging the Elastic Properties of Soft Tissues with Ultrasound

Jonathan OPHIR[1,2], S. Kaisar ALAM[1,3], Brian S. GARRA[4], Faouzi KALLEL[1], Elisa E. KONOFAGOU[1], Thomas KROUSKOP[6], Christopher R. B. MERRITT[7], Raffaella RIGHETTI[1,2], Remi SOUCHON[8], Seshadri SRINIVASAN[1,2], and Tomy VARGHESE[1,9]

Abstract

Elastography is a method that can ultimately generate several new kinds of images, called elastograms. As such, all the properties of elastograms are different from the familiar properties of sonograms. While sonograms convey information related to the local acoustic backscatter energy from tissue components, elastograms relate to its local strains, Young's moduli or Poisson's ratios. In general, these elasticity parameters are not directly correlated with sonographic parameters, i.e. elastography conveys new information about internal tissue structure and behavior under load that is not otherwise obtainable. In this paper we summarize our work in the field of elastography over the past decade. We present some relevant background material from the field of biomechanics. We then discuss the basic principles and limitations that are involved in the production of elastograms of biological tissues. Results from biological tissues in vitro and in vivo are shown to demonstrate this point. We conclude with some observations regarding the potential of elastography for medical diagnosis.

J Med Ultrasonics 2002; 29 (Winter) 155-171

Keywords

elastography, ultrasound

1. Introduction

The elastic properties of soft tissues depend on their molecular building blocks, and on the microscopic and macroscopic structural organization of these blocks (Fung 1981). The standard medical practice of soft tissue palpation is based on qualitative assessment of the low-frequency stiffness of tissue. Pathological changes are generally correlated with changes in tissue stiffness as well. Many cancers, such as cancers of the breast, appear as extremely stiff nodules (Anderson 1953). However, benign tumors of the breast may appear stiff as well, but possibly not quite as stiff as the cancers. In many cases, despite the difference in stiffness between the lesion and the surrounding normal tissue, the small size of a pathological lesion and/or its location deep in the body make its detection and evaluation by palpation difficult or impossible. In general, the lesion may or may not possess sonographic contrast that would make it ultrasonically detectable. For example, tumors of the prostate or the breast might be invisible or barely visible in standard ultrasound examinations, yet be much stiffer than the embedding tissue (Garra et al. 1997). Diffuse diseases such as cirrhosis of the liver are known to significantly increase the stiffness of the liver tissue as a whole (Anderson 1953), yet they may appear normal in conventional ultrasound examination.

Since the echogenicity and stiffness of tissues are caused by unrelated mechanisms and are thus uncorrelated, it is expected that imaging tissue stiffness, or a related parameter such as local tissue strain, will provide new information that is related to tissue morphology and architecture. This expectation has now been confirmed in the breast (Garra et al.

[1]The University of Texas Medical School at Houston, Houston, TX, USA, [2]The University of Houston, Department of ECE, Houston, TX, USA, [3]Riverside Research Institute, New York, NY, USA, [4]University of Vermont, Fletcher Allen Medical Center, Burlington, VT, USA, [5]Brigham and Women's Hospital, Boston, MA, USA, [6]Baylor College of Medicine, Houston, TX, USA, [7]Thomas Jefferson University, Philadelphia, PA, USA, [8]l'Institut National de la Sante et de la Recherche Médicale (INSERM) Unité 556, Lyon, France, [9]University of Wisconsin, Madison, WI, USA

Received on May 23, 2002; Accepted on September 13, 2002

1997, Rosenthal et al. 2002) and in animal studies (Merritt et al. 2002). In addition to pathology, we now have new evidence that various normal tissue components possess consistent differences in their stiffness parameters as well. For example, in the ovine kidney, the stiffness contrast between the cortex and the medullary pyramids has recently been measured to be only about 6 dB at low strains, and corresponding strain images showing easily discernible strain contrast have been made (Kallel et al. 1998). Similar observations have been made in the normal canine prostate, where consistent stiffness and strain contrast has been demonstrated between the outer and inner gland, and between the urethra, the verumontanum and the normal prostatic tissue (Kallel et al. 1999). These observations provide the basis for elastographic imaging the normal anatomy as well. Another observation that has been made recently in vitro is that some normal and pathological tissues may possess nonlinear stress/strain behavior (Krouskop et al. 1998). This means that their stiffnesses are a function of strain. This property may be useful in differentiating normal from abnormal tissues in the future.

Over the past 20 years there have been numerous investigations conducted to characterize the mechanical properties of biological tissue systems (Bakke 1973, Chen et al. 1996, D'Angelo 1975, Fukaya et al. 1969, Galey 1969, Gao et al. 1996, Harley et al. 1977, Malinauskas et al. 1989, Sarvazyan 1993, Yamada 1970), which have been often idealized as homogeneous, isotropic elastic materials. Much of the work has focused on bone, dental materials and vascular tissue. There are articles that discuss methods used to characterize these tissues, and there is a large volume of experimental data on the mechanical response of these tissues to various types of loading (Gao et al. 1996, Demiray 1972, Krouskop et al. 1987, Ophir et al. 1991, Ophir et al. 1996, Ophir et al. 1997, Céspedes et al. 1993). However, there is a near void in the literature regarding the mechanical properties of tissue systems tested in vivo. There is even less information available on the elastic properties of pathological tissues. Yamada's book (1970) presents a relatively broad range of data, but much of the data are derived from experiments using animal tissues and all of the information relates to results from uniaxial tensile tests of the tissue, and not from compressional tests. A recent article by Krouskop et al. (1998) provides compressional stiffness values for normal and pathological breast and prostate tissues in vitro.

The stiffness parameter is a function of the elastic modulus of the tissue and its geometry. It cannot be measured directly. A mechanical stimulus of some kind must be propagated into the tissue, and precision means for detecting the resulting internal tissue motions must be provided. Such means may include ultrasound, MRI or other diagnostic imaging modalities that can track minute tissue motion with high precision. In the last fifteen years, interest has been mounting in the ultrasonic imaging of tissue elasticity or stiffness parameters. A comprehensive literature review of this field can be found in Ophir et al. (1996) and in Gao et al. (1996). Tissue elasticity imaging methods based on ultrasonics fall currently into two main groups: 1) methods where a quasi-static compression is applied to the tissue and the resulting components of the strain tensor are estimated (Ophir et al 1991, O'Donnell et al. 1994) ; and 2) methods where a low frequency vibration (<1 kHz) is applied to the tissue, and the resulting tissue behavior is inspected by ultrasonic or audible acoustic means (Krouskop et al. 1987, Lerner and Parker 1987, Lerner et al. 1990, Yamakoshi et al. 1990, Alam et al. 1994, Fatemi et al. 1999, Walker et al., 2000).

In this review, we concentrate on describing the recent progress using the first approach that we call elastography, which has been under development in our laboratory since 1989. We first present a short summary of the theory of elasticity as it pertains to the quasi-static application of loads to biological tissues. We then give some basic tissue stiffness results that demonstrate the existence of stiffness contrast among normal tissues, and between normal and pathological tissues in the breast and prostate. We proceed to describe the elastographic imaging process, starting from the tissue elastic modulus distribution, progressing through various algorithms for precision time-delay estimation of echoes from strained tissues, and culminating in the production of the elastogram, or strain image. The use of ultrasound to acquire tissue motion information results in certain basic limitations on the attainable elastographic image quality, which may be described by the theoretical framework known as the Strain Filter (Varghese and Ophir 1997b). The Strain Filter may be used to predict and design important improvements to various elastographic image attributes, such as dynamic range expansion (Konofagou et al. 1997) and improvement in in the elastographic signal-to-noise ratio (SNRe) through multiresolution processing (Varghese et al. 1998) or compensation for undesired axial distortions (Cespedes et al. 1993) and undesired lateral tissue motion (Konofagou and Ophir 1998). In combination with certain Contrast Transfer Efficiencies (CTE) inherent in the conversion of modulus to strain contrast (Ponnekanti et al. 1995, Kallel et al. 1996), the Strain Filter formalism may be used to predict the upper-bound as well as the practically attainable Contrast-to-Noise-Ratio (CNRe) performance of elastography and its tradeoffs with elastographic resolution (Varghese and Ophir 1998, Righetti et al.

2002 a, Righetti et al. 2002 b). We conclude with some recent results that demonstrate that quality elastograms may be produced both in-vitro and in-vivo, with high contrast-to-noise ratios and at high resolutions.

2. Basic Elasticity Theory for Static Compressions

For a large number of solids, the measured strain is proportional to the load over a wide range of loads. This linear relationship is known as Hooke's law, which states that each of the components of the state of stress at a point is a linear function of the components of the state of strain at the point (Saada 1983). Mathematically, this is expressed as a constitutive equation, which may be written in tensor notation as:

$$\sigma_{kl}=C_{klmn}e_{mn},$$

where the components of the matrix C_{klmn} are elastic constants that are intrinsic properties of the material. There are generally 81 (=34) such constants, corresponding to the indices, k, l, m, and n taking values equal to 1, 2, and 3. Since both the stress tensor σ_{kl} and the elasticity tensor C_{klmn} are symmetric, the number of elastic constants reduces to 21. These constants characterize a general anisotropic, linearly elastic material. Since the elastic properties of an isotropic material are independent of the orientation of the axes, the number of elastic constant is further reduced to 3 constants which may be expressed in terms of only two independent parameters known as the Lamé's constants λ and μ. These 3 elastic constants are given by

$$C_{1122}=\lambda,\ C_{1111}=\lambda+2\mu,\ C_{121} \quad \frac{1}{2}(C_{1111} \quad C_{11} \quad \mu \tag{2}$$

The constant μ, also known as G, is referred to as the shear modulus.

The volume change per unit volume due to spherical stress is dependent on the bulk compressional modulus, K, which is related to the Lamé's constants by

$$K=\frac{3\lambda+2\mu}{3} \tag{3}$$

There are also two other engineering parameters commonly used to characterize the mechanical properties of solid materials: Young's modulus, E, and Poisson's ratio, ν. These are related to K and G by the following expressions:

$$K=\frac{}{3(} \quad \frac{E}{2\nu} \quad , \text{ and} \tag{4 a}$$

$$G \quad \frac{E}{2(1} \tag{4 b}$$

In general, soft tissues are anisotropic, viscoelastic and non-linear. However, it is usually assumed that they behave as linear, elastic, isotropic materials in order to simplify the analysis. These assumptions are likely to be reasonable for small strains, rapid load application and a spatial scale that is large compared to the relative correlation length of the elastic variability in the tissue sample (Krouskop et al. 1998).

Soft tissues contain both solid and fluid components and therefore may have mechanical properties that fall somewhere between those of both materials (Sarvazyan et al. 1995). The ratio G/K is close to a few tenths for solid materials, while it equals zero for liquids (i.e. liquids are incompressible and their Poisson's ratio equals 0.5, and from equation 1, $K \rightarrow \infty$). Many soft tissues are nearly incompressible with Poisson's ratios ranging from 0.49000 to 0.4999, which make them mechanically similar to liquids. For most solids, Poisson's ratios are between 0.2 and 0.4. Note that from equation 4 b for incompressible tissues ($\nu=0.5$), the relationship $E=3G$ holds. This means that for incompressible materials there exists a simple proportionality between the shear and the Young's moduli.

The bulk modulus K may be estimated from the propagation speed of bulk compressional waves c and the material density (ρ,i.e. $K \cong \rho c2$. Since it is well known from the literature that the dynamic ranges of the speed of sound as well as the density in soft tissues are small, the dynamic range of the bulk modulus of tissues is small as well. Hence in traditional medical ultrasound imaging, the speed of sound in tissue is assumed to be a constant 1540 m/s. Thus, the ability to create properly scaled sonograms of soft tissues is in part due to this small variability in the speed of sound. Recently, it has been shown that the shear modulus of normal and abnormal soft tissues may span much more than an order of magnitude (Sarvazyan 1993, Krouskop et al. 1998). The graphs of **Fig. 1** summarize tissue shear modulus data obtained by Krouskop et al. (1998) from different breast and prostate tissues. As can be seen, a relatively large dynamic range of the shear modulus exists in normal and abnormal breast and prostate tissues. This relatively large dynamic range of the shear modulus is responsible for the increased interest in developing new techniques for imaging information related to this modulus. By contrast, attempts to image the bulk moduli of tissues via their speeds of sound have largely been unsuccessful in the past due to the small dynamic range of this modulus and the concomitant low contrast-to-noise ratios.

It is known that the force generated by the vertical indentation of a piston into soft tissue is determined by the shear modulus (Sarvazyan et al. 1995). To illustrate this, consider the classical solution of the

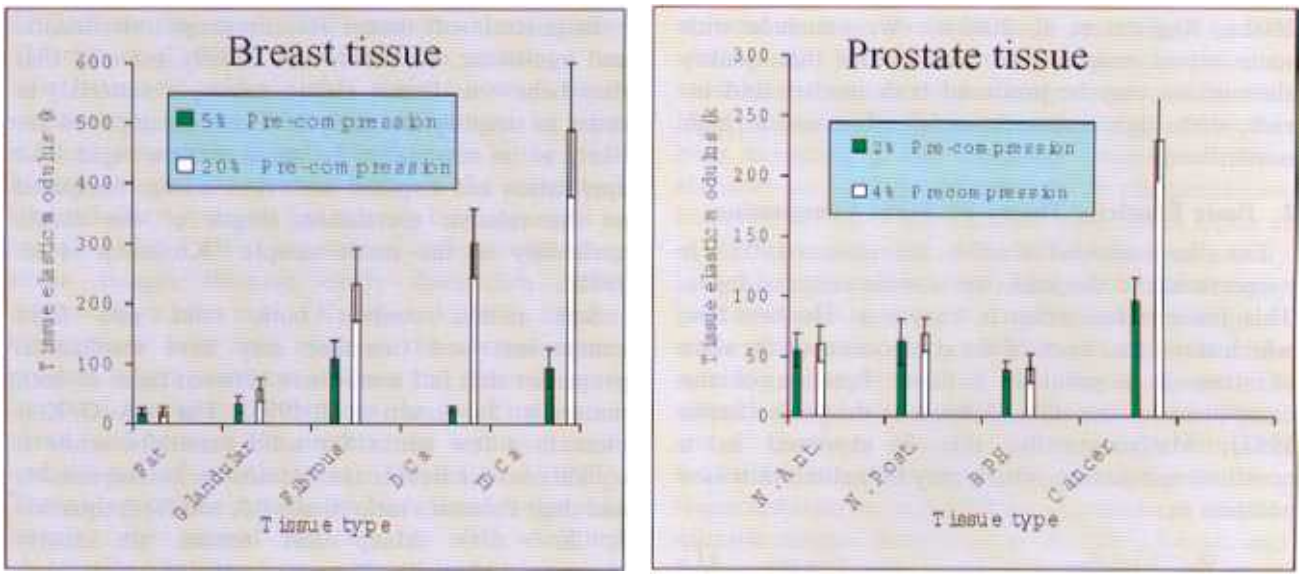

Fig. 1 Tissue elastic moduli obtained from normal and abnormal breast and prostate tissues (Krouskop et al. 1998).

force generated by the vertical displacement W of a circular piston of radius R into a semi-infinite elastic medium with shear and bulk elastic moduli G and K. This force is given by,

$$P=\frac{8GRW}{1+\dfrac{G/K}{1+G/3K,}} \tag{5}$$

where the terms containing the ratio G/K nearly vanish in soft tissues, and where $G \ll K$. Thus, the relationship between the force P and the displacement W is determined by the shear modulus and the geometry. In other words, information from manual palpation is independent of the bulk compressional modulus K. Since the force P is also related to the geometry, the stress/strain behavior measured in such an indentation experiment is generally indicative of the stiffness of the particular tissue/geometry setup, and not necessarily of the pure shear modulus of the tissue sample.

The equations describing the equilibrium-state of a linear, isotropic elastic material is given in (Sarvazyan 1993) as

$$\begin{aligned} e_{xx}&=\frac{1}{E}[\sigma_{xx}-\nu(\sigma_{yy}+\sigma_{zz})],\ e_{xy}=\frac{1+\nu}{E}\sigma_{xy} \\ e_{yy}&=\frac{1}{E}[\sigma_{yy}-\nu(\sigma_{xy}+\sigma_{zz})],\ e_{yz}=\frac{1+\nu}{E}\sigma_{yz} \\ e_{zz}&=\frac{1}{E}[\sigma_{zz}-\nu(\sigma_{xx}+\sigma_{yy})],\ e_{zx}=\frac{1+\nu}{E}\sigma_{zx} \end{aligned} \tag{6}$$

where e_{xx}, e_{yy}, e_{zz} etc. are the orthogonal strain tensor components and e_{xx}, e_{yy}, e_{zz} etc. are the corresponding orthogonal stress tensor components. In principle, for a given Poisson's ratio, any equation relating a given strain distribution to a corresponding set of stress distributions may be used to estimate the corresponding Young's modulus distribution. For example in the case of a plane-strain state problem, the modulus distribution may be obtained using the following relation

$$E=\frac{(1+\nu)(1-\nu)\sigma_{xx}-\nu\sigma_{zz})}{e_{xx}} \tag{7}$$

In general, however, only the strain distribution may be directly estimated in practice. This strain distribution is not an intrinsic tissue property. It is dependent on both internal and external boundary conditions, as well as on the distribution of shear moduli in the tissue. The external boundary conditions depend on the three-dimensional shape and relative size of the compressor compared to the tissue, as well as on the degree of friction between the internal and external contact surfaces. The shape and type of the tissue components determine the internal boundary conditions. Therefore, a map of the strain distribution in tissue reveals not only information about tissue shear modulus distributions, but also about tissue connectivity (interfaces between tissue components) and other geometrical considerations. Alternatively, the map may be designated as a stiffness distribution, which includes the effects of the modulus and the geometry. An incorrect interpretation of the stiffness distribution as being the shear modulus distribution may in some cases result in some known image artifacts due to stress concentrations that may be misinterpreted as areas of low modulus. However, we have previously

demonstrated (Kallel et al. 1998) that for low modulus contrast and simplified geometrical boundary conditions, the stiffness distribution may be a relatively good representation of the underlying modulus distribution.

3. Elastography—Imaging Tissue Strain

When a constant uniaxial load deforms an elastic medium, all points in the medium experience a resulting level of longitudinal strain whose principal component is along the axis of compression. If one or more of the tissue elements has a different stiffness parameter than the others, the level of strain in that element will generally be higher or lower; a stiffer tissue element will generally experience less strain than a softer one. The longitudinal axial strain is estimated in one dimension from the analysis of ultrasonic backscattered signals obtained from standard diagnostic ultrasound equipment. This means that ultrasonic speckle may be used for this purpose, and no discrete resolvable targets must be present. This estimation is accomplished by acquiring a set of digitized radio-frequency echo lines from scatterers contained in the tissue region of interest; compressing the tissue with the ultrasonic transducer (or with a transducer/compressor combination) along the ultrasonic radiation axis by a small amount (generally about 1% or less of the total tissue depth), and; acquiring a second, post-compression set of echo lines from the same region of interest. Congruent echo lines are then subdivided into small temporal windows that are compared pair-wise by using one of a variety of possible known time-delay estimation techniques such as cross-correlation, from which the change in arrival time of the echoes before and after compression can be estimated. Due to the small magnitude of the applied compression, there are only small distortions of the echo lines, and the changes in arrival times are also small. The local longitudinal strain under the assumption of constant speed of sound is estimated as the gradient of the displacement, viz.

$$e_{11,local} = \frac{(t_{1b} - t_1) - (t_{2b} - t_{2a})}{t_{1b} - t_{1a}}, \qquad (8)$$

where t_{1a} is the arrival time of the pre-compression echo from the proximal window; t_{1b} is the arrival time of the pre-compression echo from the distal window; t_{2a} is the arrival time of the post-compression echo from the proximal window; and t_{2b} is the arrival time of the post-compression echo from the distal window. **Fig. 2** shows a schematic representation of the time delay and strain computation process. The windows are usually translated in small overlapping steps along the temporal axis of the echo line, and the calculation is repeated for all depths. The fundamental assumption

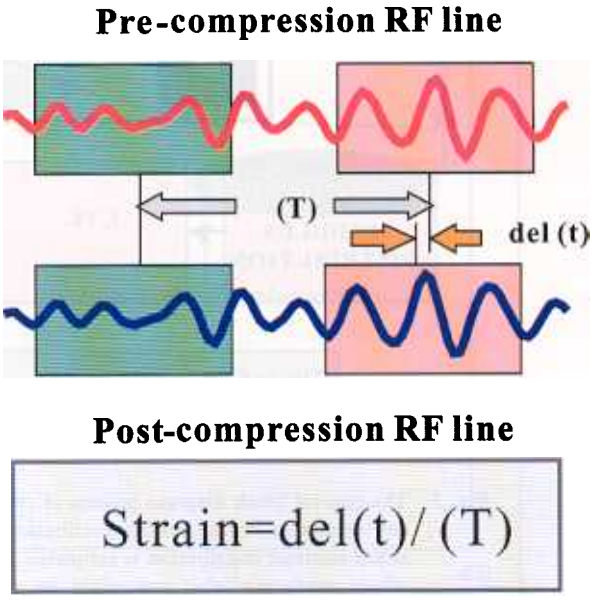

Fig. 2 A schematic showing the process of computing the strain in a tissue segment. Congruent windowed segments of the pre-compression and post-compression signals are compared by crosscorrelation. While the early windowed segments exhibit virtually no delay, a finite delay (designated del (t)) is detected between the later segments. The strain is computed as the gradient of the time delay (or displacement), i.e. strain = del (t) /T, where T is the initial (pre-compression) separation between the windowed segments.

made is that speckle motion adequately represents the underlying tissue motion for small uniaxial compressions. This assumption appears to be reasonable as long as the distributions of the scatterers before and after compression remain highly correlated. We have shown recently (Konofagou and Ophir 1998) that the lateral motion of the scatterers due to tissue compression may also be estimated with high precision using novel interpolation techniques operating on signals obtained from two partially overlapped beams. This allows the generation of elastograms that depict the lateral tensor components of the strain and at least partial re-correlation of the signals prior to the computation of the axial strains, resulting in better elastographic image quality, and/or the generation of elastograms depicting the local ratios of the lateral-to-axial strains (effectively, the Poisson's ratio)

The general process of creating elastograms is shown in **Fig. 3**, showing a block diagram of the process. The first block of the process corresponds to an example of a uniform target containing a simple circular pattern of higher tissue modulus. The intermediate block corresponds to the ideal strain distribution in the target due to the behavior of this target under a compressive load. The transformation from modulus contrast (first block) to strain contrast

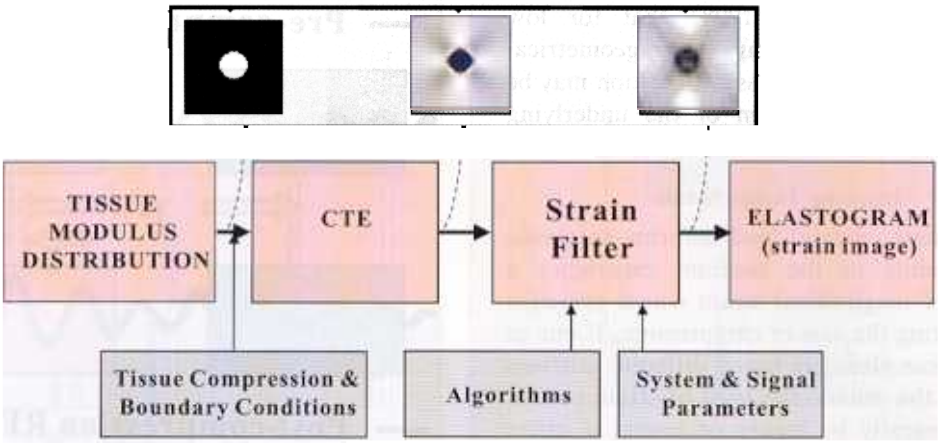

Fig. 3 The general block diagram process of creating an elastogram. The modulus contrast distribution is converted to a strain contrast distribution using the Contrast-Transfer Efficiency (CTE). The ideal strain contrast distribution is estimated from ultrasonic strain estimates by the ultrasound system, whose performance is controlled by the derated Strain Filter (SF) for particular acoustic, instrumentation and algorithmic parameters. The result is an estimated strain contrast distribution (elastogram), which is a somewhat corrupted version of the ideal strain image.

(second block) involves a certain loss of efficiency. This may be computed for such simple targets by the Contrast Transfer Efficiency (CTE) function. The output image corresponds to the strain (axial and/or lateral) image (elastogram), which is a corrupted (noisy) version of the ideal strain image. The noise and contrast properties of the elastogram are computed from the Strain Filter (SF), which takes into account the engineering, signal processing and acoustical parameters that corrupt the ideal strain image and limit the ultimate quality of the attainable elastogram. The block describing the instrument incorporates the Strain Filter (Varghese and Ophir 1997 b), which embodies the selective filtering of the tissue strains by the ultrasound system and signal processing parameters. The SF predicts a finite dynamic range and respective elastographic signal-to-noise ratio (SNRe) at a given resolution in the elastogram, limited by noise and/or decorrelation. The contributions of the signal processing and ultrasound system parameters and other algorithms are indicated as inputs into the SF. Combining the CTE and the SF formulations leads to the description of the elastographic contrast-to-noise ratio (CNRe) in the elastogram. All these blocks are described later in this article. A complete description may be found in Ophir et al (1999).

4. Contrast-Transfer Efficiency (CTE)

Using ultrasonic techniques, it is only possible to measure some of the local longitudinal components of the strain tensor in the tissue. The local components of the stress tensor remain largely unknown. The strain elastogram is all that is available to represent the distribution of tissue elastic moduli, if this is indeed what is desired. The CTE is defined as the ratio of the observed (axial) strain contrast ratio Co measured from the strain elastogram, and the underlying true modulus contrast ratio Ct, using a plane-strain state model. Expressed in decibels, the ratio becomes a difference that is given by:

$$CTE(\mathrm{dB}) = |C_o(\mathrm{dB})| - |C_t(\mathrm{dB})|, \qquad (9)$$

where the magnitude is used in order to have CTE normalized to the zero dB level; i.e. the maximum efficiency is reached at 0 dB for both hard and soft inclusions. This behavior has been verified by finite-element simulations and was also corroborated theoretically, using models of simple geometry (Ponnekanti et al. 1995, Kallel et al 1996). **Fig. 4** shows the behavior of the CTE parameter over an 80 dB dynamic range of modulus contrast as measured from simulated data (data points), and as predicted using an analytical model (smooth curve). It is clear from the Figure that for low modulus contrast levels (a high level of target modulus homogeneity), the elastographic strain contrast is relatively close to the modulus contrast (the contrast transfer efficiency CTE $\approx$ 1, or 0 dB). This is a very important observation, since it suggests that for tissues that have structures that possess low modulus contrast, the simply computed axial strain elastogram itself is very similar to the inverse of the true shear modulus distribution in the tissue. This expected result has been verified experimentally using actual indentation measurements and elastograms, using ex-vivo ovine kidneys and phantoms (Kallel et al. 1998). Hard inclusions embedded in softer background have a relatively high level of contrast-transfer efficiency (CTE $\approx$ 0 dB). However, soft inclusions that are

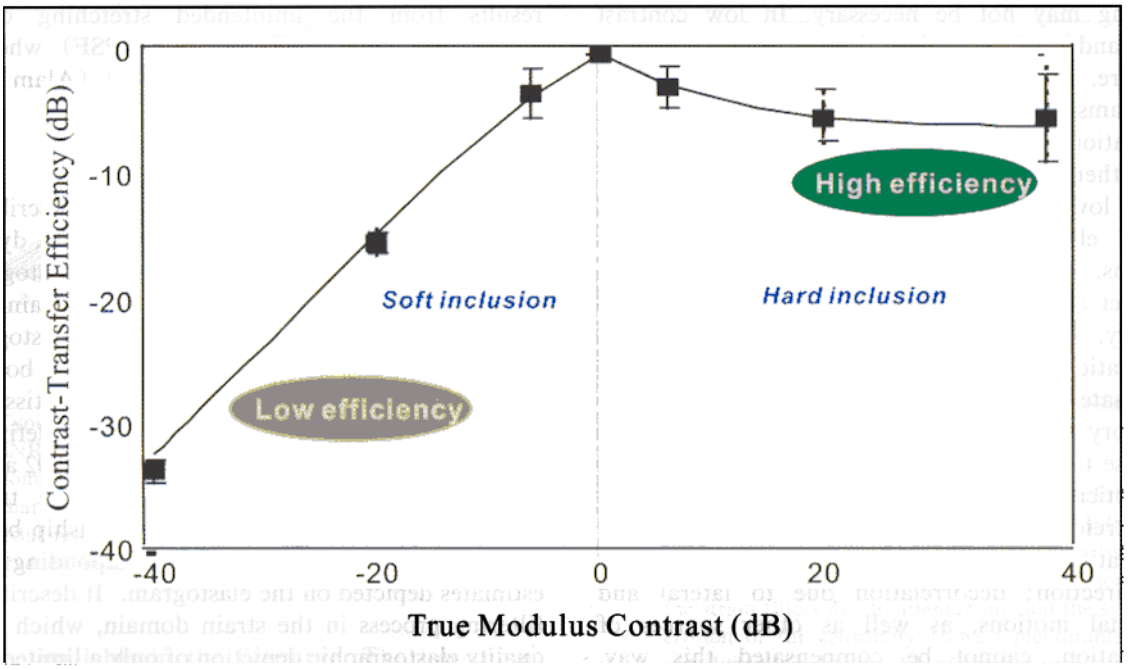

Fig. 4 The behavior of the Contrast Transfer Efficiency function for a plane-strain-state circular inclusion. Note that the strain contrast is close to the modulus contrast (and hence the efficiency is high, i.e., CTE=1, or 0 dB) for low ($\ll$0 dB) modulus contrast lesions. Note also that the function is asymmetric, demonstrating high efficiency for stiff inclusions, and low efficiency for soft inclusions.

completely surrounded by harder background material have low contrast-transfer efficiency (CTE $\ll$0 dB), and thus may not be well visualized by elastography. The reason for this limitation lies in the fact that due to the incompressible nature of many soft tissues (Poisson's ratio$\sim$0.5), the soft inclusion will be constrained so that it will be unable to deform under load, as it might otherwise do without constraints. It will thus assume instead effective elastic properties that are closer to those of the embedding, stiffer material.

5. Time Delay Estimation (TDE) in Strained Tissues

Time delay estimation is a very important aspect of elastography. The literature on TDE is extensive. Tissue strain is typically estimated from the axial gradient of tissue displacements. The local tissue displacements are estimated from the time delays of gated pre-compression and post-compression echo signals. Time delays are classically estimated from the lag of the peak of the crosscorrelation function between the pre- and post-compression gated echo signals. It is also possible to use other estimators of time delay, such as the frequency shift of the cross-spectrum (Konofagou et al. 1999), or the point of zero phase of the crosscorrelation function (Pesavento et al 1999, Lorenz et al. 2001).

The quality of elastograms is highly dependent on the optimality of the TDE estimation procedure. TDE in elastography is mainly corrupted by two factors. First, random noise introduces errors in the TDE, which are especially disruptive at small time delays. Second, since the tissue needs to be compressed to produce elastograms, this very same compression of the tissue also distorts the post-compression signal such that it no longer is an exact delayed version of the pre-compression signal. This decorrelation increases with increasing strain and is independent of the signal-to-noise ratio of the echo signals. Any phenomenon (such as lateral and elevational motion) that degrades the precision of the time-delay estimates will also degrade the strain estimates, thus introducing additional noise into the elastogram.

Echo signal decorrelation is one of the major limiting factors in strain estimation and imaging. For small strains, it has been shown that temporal stretching of the post-compression signal (or temporal compression of the pre-compression signal) by the appropriate factor can almost entirely compensate for signal decorrelation. When the post-compression echo signal is stretched, it in effect realigns all the scatterers within the correlation window. Global uniform stretching was found to significantly improve the elastographic signal-to-noise ratio (SNRe) and expand the strain dynamic range in elastograms (Alam and Ophir 1997). Moreover, this step is computationally simple. Thus, a global uniform stretching of the post-compression A-line prior to the displacement estimation is highly advisable, unless the applied compression is very small ($\ll$1%) and thus

stretching may not be necessary. In low contrast targets and/or low strains, this is a very effective procedure. In these situations, it produces quality elastograms without significantly adding to the computational load. However, in high contrast targets, there will be significant over-stretching in the areas of low strains, which by itself can significantly degrade elastograms in these areas. For these situations, an adaptive axial stretching algorithm (Alam et al. 1998 b, Brusseau et al. 2000) may be necessary. If high strains are applied, significant decorrelation occurs, which cannot effectively be compensated by stretching. Axial stretching is mandatory in the presence of intermediate strains; otherwise the elastograms become so noisy that they are practically useless. It must be remembered that axial stretching can only recover most of the decorrelation suffered due to scatterer motion in the axial direction; decorrelation due to lateral and elevational motions, as well as other sources of decorrelation, cannot be compensated this way. Konofagou and Ophir (1998) have demonstrated that decorrelation due to lateral motion may be compensated with high accuracy by using a signal interpolation technique. This technique, when applied alternately with axial stretching, was shown to result in large improvements in elastographic image quality. A deconvolution filtering approach may be useful in reducing the remaining decorrelation that results from the unintended stretching of the transducer point-spread function (PSF) when the post-compression signal is stretched (Alam et al. 1998 a).

6. The Strain Filter (SF)

The SF (Varghese and Ophir 1997 b) describes the important relationship among the resolution, dynamic range (DRe), sensitivity (Smin) and elastographic SNRe (defined as the ratio of the mean strain to the standard deviation of the strain in the elastogram), and may be plotted as a graph of the upper bound of the SNRe vs. the strain experienced by the tissue, for a given elastographic axial resolution (as defined by the data window length (Righetti et al. 2002 a). The SF is a statistical upper bound of the transfer characteristic that describes the relationship between actual tissue strains and the corresponding strain estimates depicted on the elastogram. It describes the filtering process in the strain domain, which allows quality elastographic depiction of only a limited range of strains from tissue. This limited range of strains is due to the limitations of the ultrasound system and of the signal processing parameters and algorithms. The SF is obtainable as the ratio between the mean strain estimate and the appropriate lower bound on its standard deviation. On a logarithmic scale, this ratio is seen as a difference (**Fig. 5**). The SF is based on well-known theoretical lower bounds on the TDE

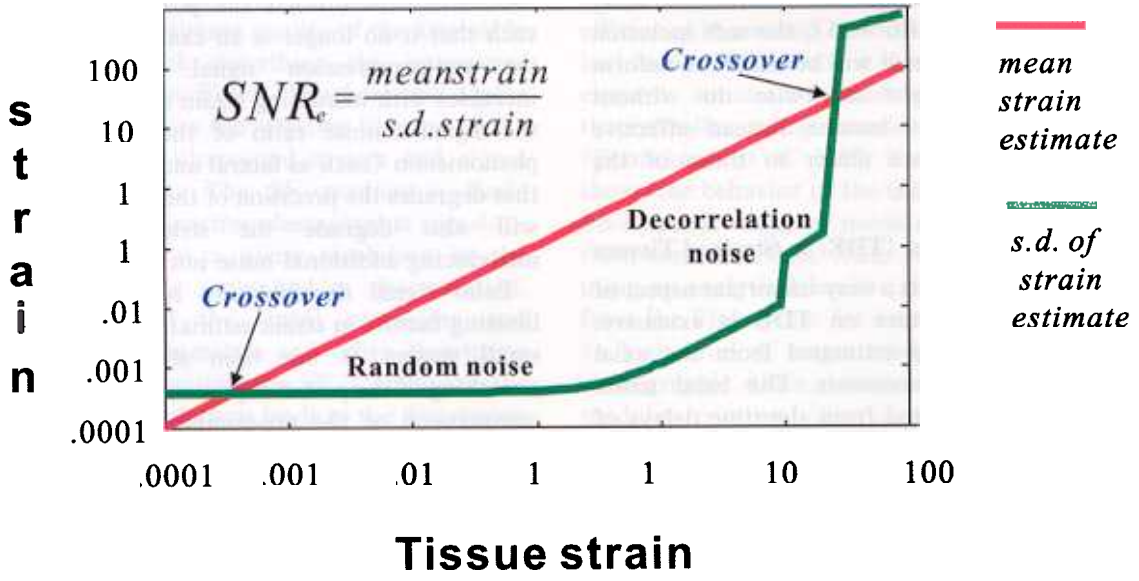

Fig. 5 Mean strain estimate and standard deviation of the strain as a function of the applied strain. Observe that while the mean estimate is proportional to the tissue strain, the behavior of the standard deviation (s.d.) is highly nonlinear. At low strains, the s.d. is constant and low, and is determined by the Cramer-Rao Lower Bound (CRLB). At higher strains, phase ambiguities in the signal cause a sharp increase of the s.d. The ratio of the mean to the lower bound of the s.d. of the strain estimate, as a function of tissue strain, is defined as the Strain Filter. In logarithmic units, the ratio is simply the difference between the two curves. Hence it is expected that the Strain Filter will have a bandpass characteristic, where the SNRe is low at low and high strains, and high at intermediate strains between the crossover points.

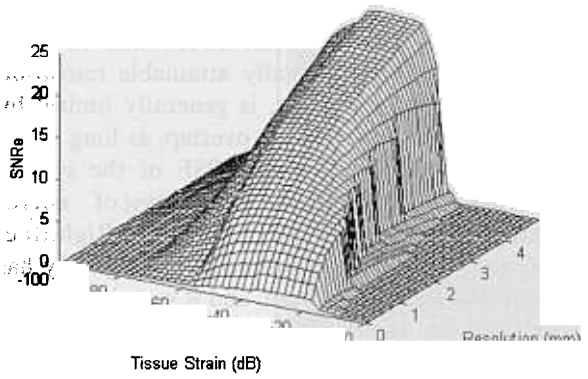

Fig. 6 Typical appearance of the strain filter. Observe that the SNRe has a bandpass characteristic in the strain domain, and the magnitude of this bandpass characteristic is diminished at higher (smaller valued) axial resolutions. Hence, for a given strain, there is a tradeoff between SNRe and axial resolution.

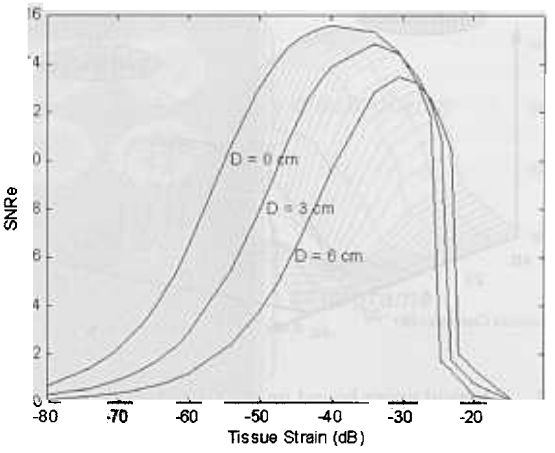

Fig. 7 A typical appearance of a family of Strain Filters at a fixed axial resolution. The member Strain Filters have been derated to account for attenuation in tissue at 3 cm and 6 cm depths. Note the axial nonstationarity of the strain filters due to attenuation, and the systematic erosion of the sensitivity (lowest measurable strain) and dynamic range (width of the Strain Filter) of the strain in the elastogram.

variance, available in the literature. The low-strain behavior of the SF is determined by the variance as computed from the Cramér-Rao Lower Bound (CRLB) (modified for partially correlated signals). The high-strain behavior of the SF is determined by the rate of decorrelation of a pair of congruent signals due to tissue distortion as shown in **Fig. 5, 6** illustrates the general appearance of the SF in three dimensions, demonstrating the tradeoffs between SNRe and strain at all resolutions. An important extension to the SF is its combination with the CTE formalism to produce elastographic Contrast-to- Noise (CNRe) vs. strain curves. This allows the description of the CNRe of simple elastic inclusions or layers in terms of both the mechanical strain contrast limitations in the target, and the noise properties of the apparatus.

6.1 Nonstationarity of the Strain Filter

Estimation of tissue strains is inherently a nonstationary process, since the pre- and post-compression RF echo signals are jointly nonstationary (due to signal deformation caused by straining tissue). However, the pre- and post-compression signals can be approximated to be jointly stationary, if the tissue strain is estimated using small windowed data segments in conjunction with temporal re-stretching of the post-compression signal. Frequency dependent attenuation causes additional (axial) nonstationarity into the strain estimation process vs. depth (Varghese and Ophir 1997 a), while lateral and elevational signal decorrelation introduce nonstationarities in the strain estimation process along the lateral and elevational directions respectively (Kallel et al. 1997). The SF can be derated by these corrupting processes to predict the effect of these nonstationarities on the elastogram. For example, The effect of lateral decorrelation contributes predominantly to the nonstationary variation in the SNRe . Both the SNRe and the dynamic range are reduced with an increase in lateral decorrelation. As long as any stationary or nonstationary additive noise source can be described, its effect may be incorporated into the Strain Filter formalism, resulting in a more realistic, derated (sub optimal) Strain Filter. An example of a successively derated Strain Filter due to increasing tissue attenuation at larger depths (in two dimensions only (at a fixed resolution)) is shown in **Fig. 7**.

6.2 Contrast-to-noise Ratio in Elastography

The contrast-to-noise ratio (CNRe) in elastography is an important quantity that is related to the detectability of a lesion. The properties of the ultrasound imaging system and signal processing algorithms described by the SF can be combined with the elastic contrast properties (CTE) of tissues with simple geometry, enabling prediction of the elastographic contrast-to-noise ratio (CNRe) parameter. This combined theoretical model enables prediction of the elastographic CNRe for simple geometry such as layered (1-D model) or circular lesions (2-D model) embedded in a uniformly elastic background. An upper bound on the CNRe may be obtained using the Fisher discriminant statistic, viz.:

$$CNR_e = \frac{2(s_1 - s_2)^2}{\sigma_{s1}^2 + \sigma_{s2}^2} \qquad (10)$$

The CNRe for specific geometry that possess an analytic or experimental CTE description can be obtained (Varghese and Ophir 1998) by substituting the strains obtained using the elasticity model and their respective variances from the SF into Eq. (10).

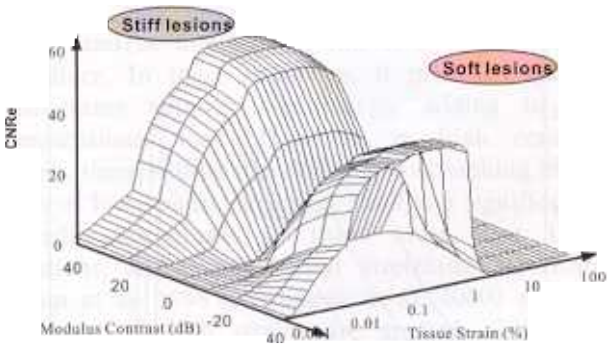

Fig. 8 A typical upper bound on the elastographic Contrast-to Noise ratio (CNRe) as a function of modulus contrast and strain. This function (nicknamed the "Opera House") is obtainable by combining the CTE and SF formalisms.

Fig. 8 illustrates the general appearance of the upper bound on the CNRe, demonstrating the tradeoffs among CNRe and modulus contrast for all applied strains. Note from **Fig. 8** and Eq. (10) that the highest values of the CNRe are obtained where two conditions are satisfied; firstly, the differences in mean strain values must be large, and secondly the sum of the variances of the strain estimates should be small. The improvement of the CNRe at low modulus contrasts is primarily due to the small strain variances, while at high modulus contrasts the improvement in the CNRe is due to the large difference in the mean strains. Note from the 3-D visualization of the CNRe curves in **Fig. 7**, that when the differences in the mean strain values are small (in the region around the middle of the graph at low contrasts), the CNRe value obtained is close to zero. In addition, the regions with large strains (corresponding to large variances in the strain estimate due to signal decorrelation) also contribute to low CNRe values. Knowledge of the theoretical upper bound on the CNRe in elastography is crucial for determining the ability to discriminate between different regions in the elastograms. The CTE for the elasticity models and the elastographic noise characterized by the SF determine the CNRe in elastography. The 3-D visualization of the CNRe curves illustrate the strain dependence of the elastographic CNRe .The 3-D plot provides a means of maximizing the CNRe in the elastogram for the given ultrasound system and signal processing parameters.

6.3 Resolution in Elastography

It has recently been demonstrated (Righetti et al. 2001) that the upper bound on the elastographic axial resolution is proportional to the length of the point-spread-function (PSF) of the transducer. The constant of proportionality depends on the exact definition that is used for the axial resolution, but is generally a number between 1 and 2. This limit is not always achieved (Alam et al. 2000) due to noise considerations.. The practically attainable resolution for a given system, however, is generally limited by the choice of window size and overlap, as long as the window size is larger than the PSF of the system. This bodes well for the feasibility of micro-elastographic imaging at high frequencies (Righetti et al. 2002 a). The lateral resolution of elastography has also been investigated in detail, and it was shown to be proportional to the beamwidth of the transducer (Righetti et al. 2002 b). Hence the best achievable spatial resolutions of elastography and sonography are similar, which means that comparisons between sonograms and elastograms may be made on a similar scale and with good registration.

7. Applications of Elastography

In principle, elastography may be applied to any tissue system that is accessible ultrasonically and which can be subjected to a small static (or dynamic) compression. The compression may be applied externally or internally. Any physiological phenomena, such as pulsating arteries or respiration, may be used as a source of tissue compression. In this section a summary of results from some of these applications is presented.

A typical example of the elastographic visualization of a canine prostate in vitro is shown in **Fig. 9**. In the elastograms, the white (stiff) rim, depicted in both the transverse and sagittal views and in each slice, corresponds to the outer gland that surrounds a softer (gray) inner gland. In the center of the prostate, the verumontanum is elastographically demonstrated as a small stiff (white) ridge along the urethra. The lumen of the urethra is depicted as a soft (black) inverted "V" or "U" shaped area. By comparison, the companion sonograms do not provide a clear visualization of the aforementioned anatomical structures in the prostate. It should be noted that the each elastogram was derived from two of very similar sonograms, one of which is shown.

The first in vivo application of elastography was to the imaging of the breast and skeletal muscle (Céspedes et al. 1993). An example of the visualization of breast carcinoma is given in **Fig. 10**. Both the B-scan and the corresponding elastogram show a large lesion at 3 o'clock. The size of this lesion on the elastogram is larger compared to its size on the corresponding sonogram. The elastogram also depicts a second, much smaller lesion at 11 o'clock, which is not demonstrated in the sonogram. Both lesions were pathologically confirmed. Further work has demonstrated that unlike benign breast tumors, cancers were consistently larger on the elastogram compared to their corresponding size on the sonogram. This size discrepancy was hypothesized to

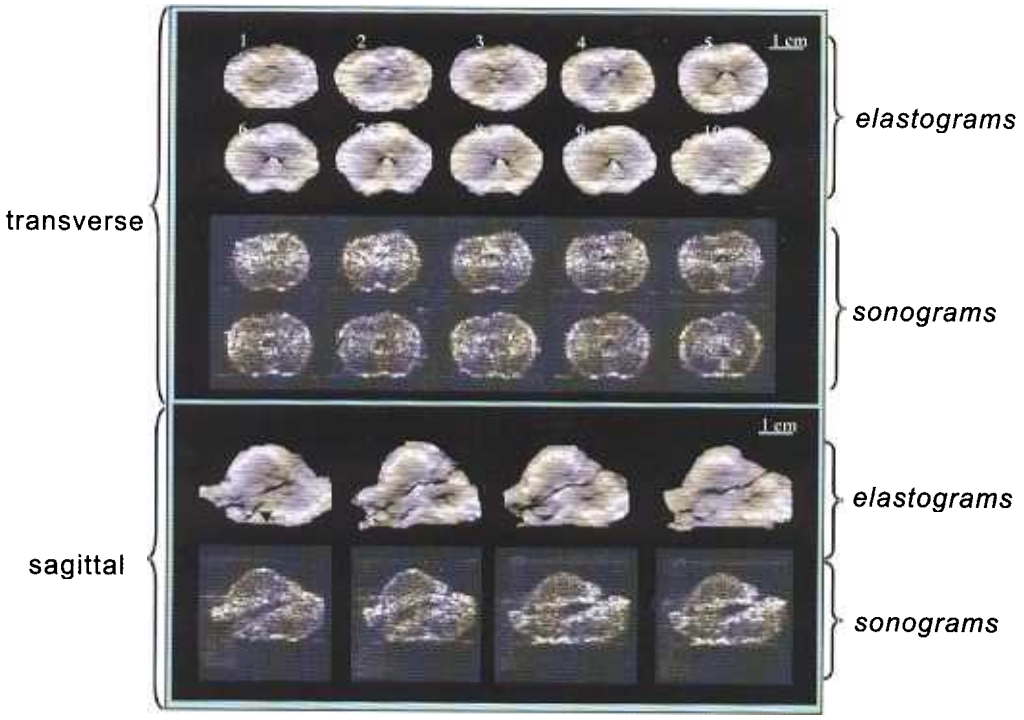

Fig. 9 Matching elastograms and sonograms obtained from 1 mm equally spaced parallel transverse and sagittal cross-sections of a typical canine prostate at 5 MHz. The prostate size is approximately $3 \times 3 \times 3$ cm^3. The elastograms are displayed using a reversed gray-scale map where white means stiff and black means (Kallel et al. 1999). Note the clear depiction of the urethra, consistently stiffer outer gland and softer inner gland, the soft acini and the stiff verumontanum in the corresponding elastograms.

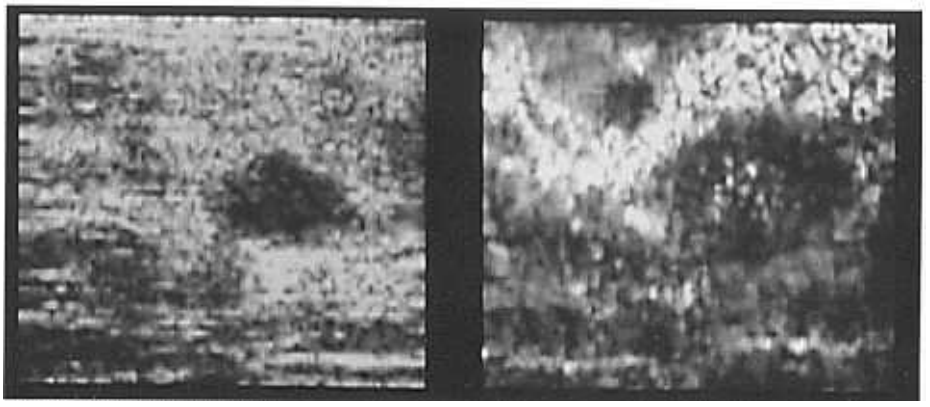

Fig. 10 From left to right, matching sonogram and elastogram of breast carcinomas obtained in vivo in the erect position at 5 MHz (Ophir et al 1996). Note the demonstration of two hard nodules and the torturous soft subcutaneous fat layer on the elastogram. Note also that the sonogram demonstrates only one hypoechoic nodule and that a size discrepancy exists between the sonographic and elastographic appearance of the large nodule (presumably due to desmoplasia). (Courtesy of Dr. Nabil Makled).

be associated with desmoplasia surrounding the cancerous lesion.

The earliest breast images were obtained in a sitting position, which limited the number of accessible cancers for elastographic imaging. More recently, breast elastograms were obtained in the supine position, which allowed the imaging of cancers that were close to the chest wall. An example of elastograms and corresponding sonograms of a fibroadenoma and a carcinoma (Garra et al. 1997) obtained in the supine position is shown in **Fig. 11**. Observe the size discrepancy between the sonographic and elastographic appearance of the carcinoma.

Another example of the visualization of normal

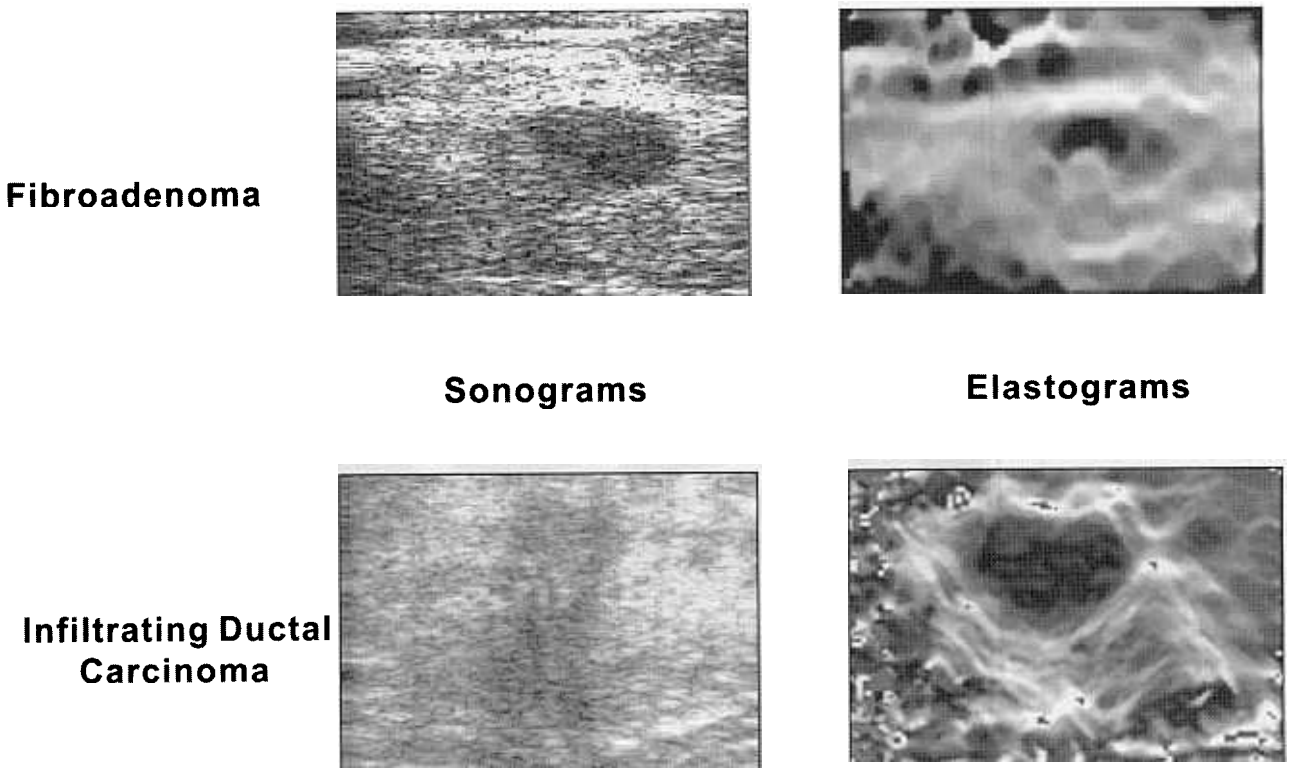

Fig. 11 Sonogram and elastogram pairs from fibroadenoma and infiltrating ductal carcinoma (Garra et al. 1997) of the breast (Courtesy of Dr. B. Garra) in vivo at 5 MHz. Observe the clear depiction of the carcinoma on the elastogram (including the distal margins), as well as the size discrepancy between the sonographic and elastographic appearance of the carcinoma, as shown also in Fig. 10.

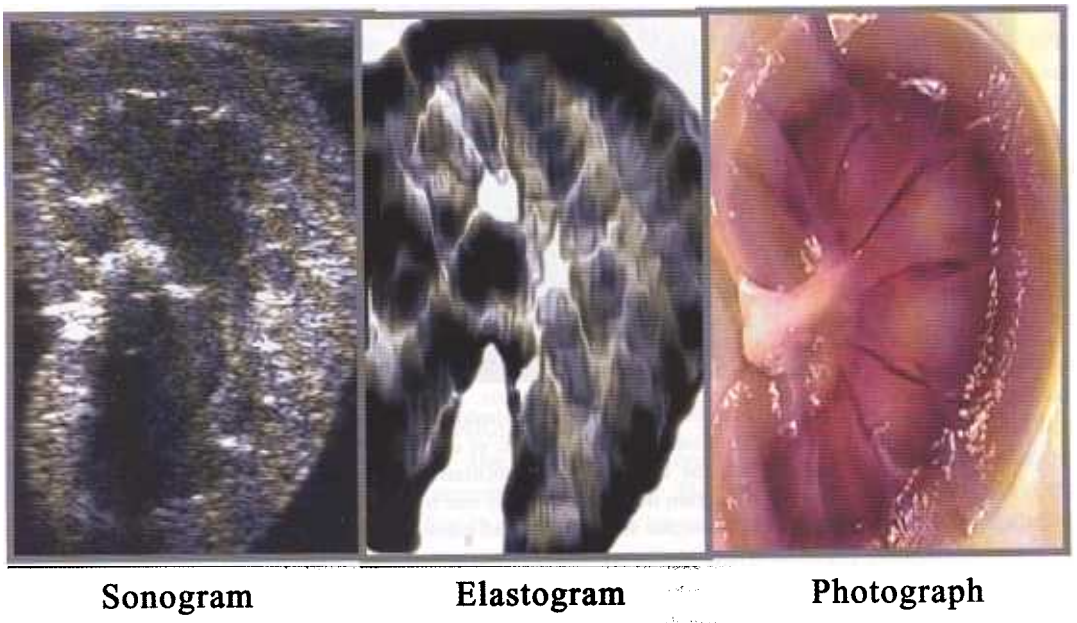

Fig. 12 From left to right, longitudinal sonogram, elastogram and gross pathological specimen from an ovine kidney in vitro. The elastogram demonstrates structures that are consistent with a stiff (black) renal cortex and medullary pyramids (of which at least seven are seen), softer (white) columns of Bertin and very soft fatty areas at the base of the columns in the renal sinus. Areas of sonographic echo dropouts outside the kidney and in the acoustically shadowed areas distal to the renal sinus are intentionally blanked in the elastogram. Note that the renal sinus is hypoechoic and is not well visualized on the sonogram (Kallel et al. 1998).

tissue architecture is shown in **Fig. 12**. The panels show an ovine kidney in-vitro as seen in a sonogram (left), elastogram (center), and gross pathological slice. It is evident that elastography may be able to demonstrate normal tissue structures, such as the pyramids and columns of Bertin, that are not well visualized on the sonogram.

Elastography has shown promise for monitoring tissue stiffening due to thermal ablative procedures. An example of the visualization of HIFU lesion induced in a canine liver in vitro is shown in **Fig. 13**, where the lesion appears as a hard nodule. It is noted that the sonogram does not demonstrate the lesion. An example of prostate trans-rectal elastography in vivo incorporating HIFU effects (Souchon et al. 2001) is shown in **Fig. 14**, where an ablated area is

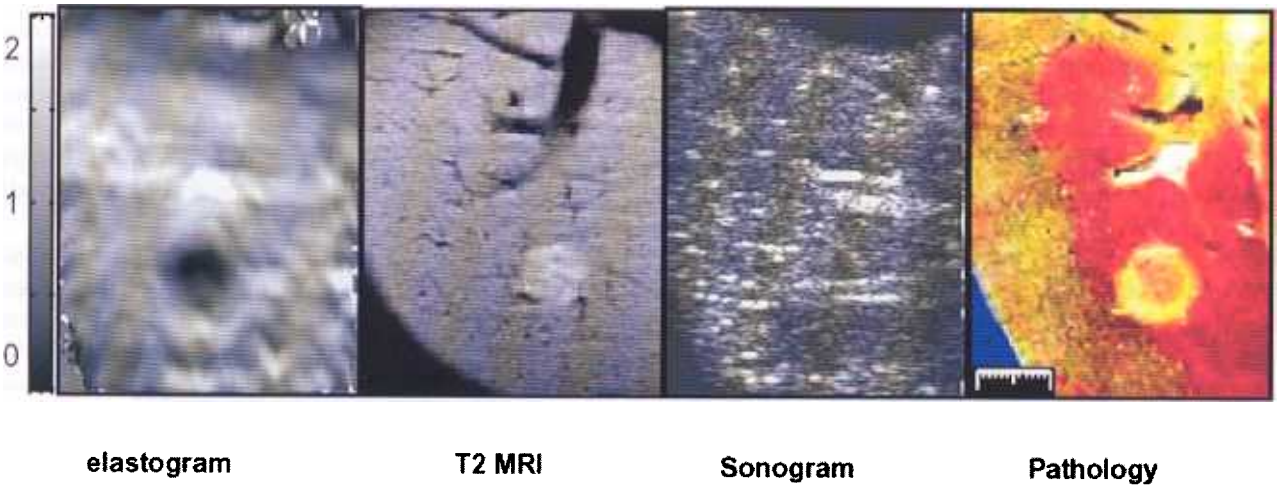

Fig. 13 From left to right: elastogram, sonogram, coronal T2-weighted-MR image and gross (stained) pathological specimen of a HIFU lesion induced in a canine liver in vitro. Note that the sonogram does not demonstrate the HIFU lesion (Righetti et al. 1999).

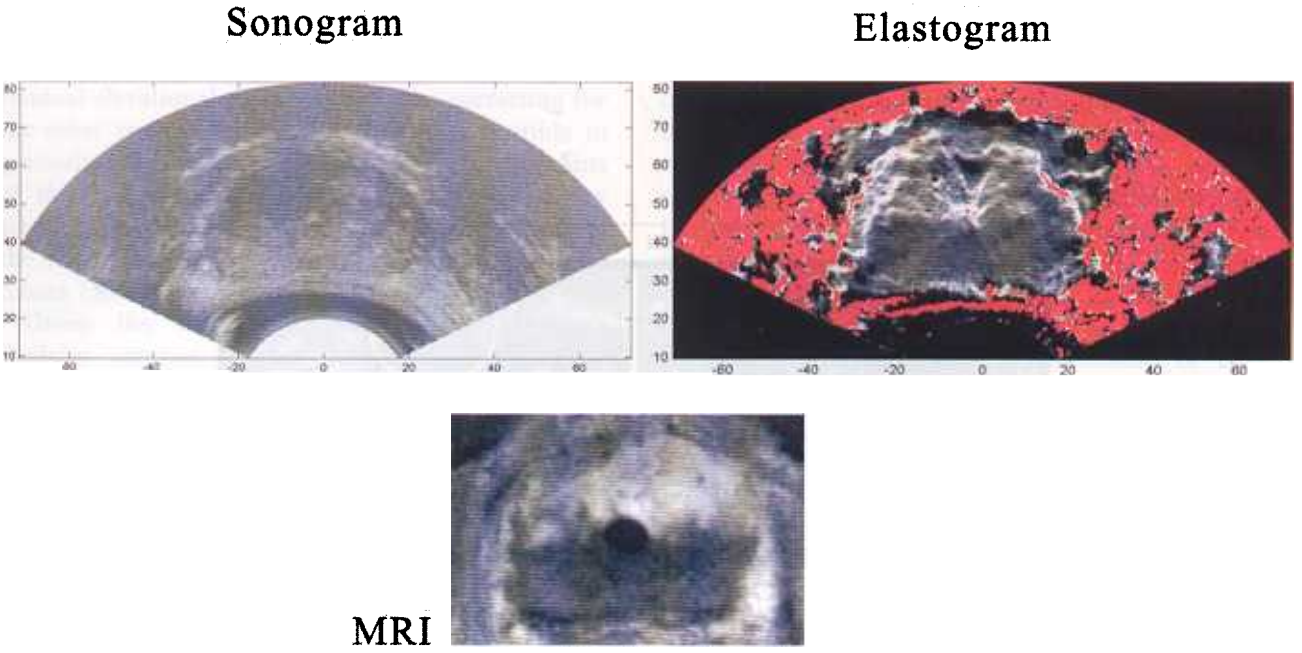

Fig. 14 Matching sonogram, elastogram and MRI image of the transverse prostate in vivo. The prostate has undergone HIFU ablation in the lower half of the gland. The rectangular ablated region is visible as a stiff region in the elastogram, and is also well shown in the MRI image. The red regions in the elastograms have been automatically added to mask out extra-prostatic regions of high decorrelation noise due to undesired tissue motions. No echo contrast between the ablated and normal parts of the prostate is shown on the sonogram (Souchon et al. 2001, unpublished).

shown as a stiff (darker) area in the peripheral proximal area of the gland, and is confirmed by MRI imaging.

Some work in animals in vivo is shown in **Fig. 15, 16** (Merritt et al. 2002). **Fig. 15** shows the appearance of a 3 mm thermal lesion created in the liver of a rabbit. Note the clear visualization of the lesion as a stiff (dark) region in the elastogram, and the corresponding isoechoic appearance on the sonogram.

Fig. 16 shows the appearance of a 6 mm VX2 carcinoma in a rabbit liver. Note again the clear appearance of the tumor as a stiff region, and the lack of tumor contrast in the corresponding sonogram.

8. Discussion and Conclusion

The assumption driving the development of elastography has been that significant soft tissue modulus (and hence strain) contrast exists, especially

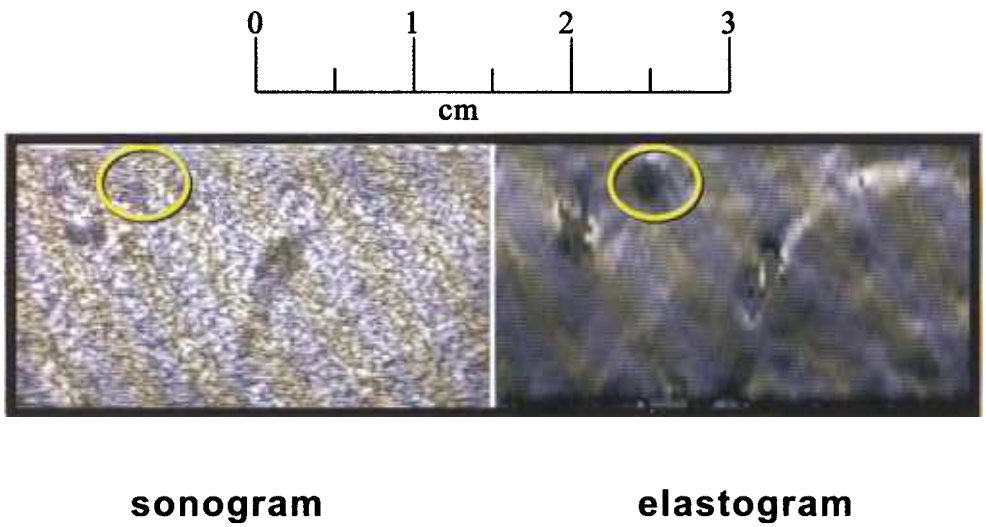

Fig. 15 Rabbit liver in vivo, bearing a 3 mm thermal lesion. Note the good contrast between the stiff lesion and the embedding normal liver in the elastogram, and the lack of echo contrast in the sonogram. The sonograms were taken with a Philips/ATL HDI-1000 scanner at 7.5 MHz (Merritt et al., 2002).

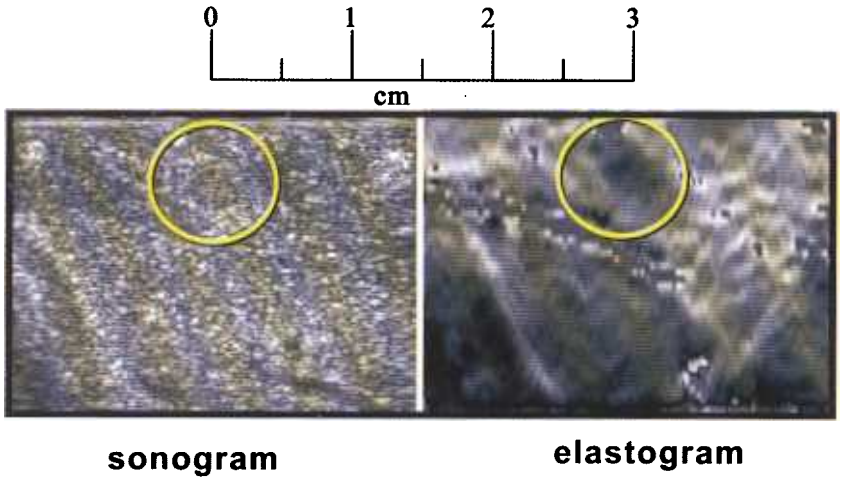

Fig. 16 Rabbit liver in vivo, bearing a 6 mm VX2 carcinoma. Note the good contrast between the stiff carcinoma and the embedding normal liver in the elastogram, and the lack of echo contrast in the sonogram. The sonograms were taken with a Philips/ATL HDI-1000 scanner at 7.5 MHz (Merritt et al.. 2002).

between normal and abnormal tissues. Perhaps not surprisingly, it has been recently demonstrated that modulus contrast exists not only between normal and pathological tissues, but also generally to a lesser degree also between and within normal tissues. The existence of this lower contrast could be ascertained only after recent vast improvements in the elastographic image quality due to a better understanding of the theory of elastographic image formation that led to the development of better algorithms. These observations, together with some initial clinical data showing the ability of elastography to detect and characterize sonographically occult breast cancers (Garra et al. 1997), are providing the catalyst for continuing the vigorous development and application of elastographic methods to medical imaging problems.

The estimation and imaging of tissue strains is by definition a three-dimensional problem. When the tissue is compressed, the near incompressibility of most soft tissues means that finite strain tensor components are generated in all directions simultaneously. Until recently, workers in the field had assumed that single-view ultrasonic methods could not be used for precision lateral displacement and strain estimates. As a result, they were essentially limited to displacement and strain estimations in the axial direction only. It has recently been demonstrated (Konofagou and Ophir 1998) that it is in fact possible to make precision estimations of lateral displacements and produce images of lateral strain and Poisson's ratio distributions in tissues, if proper overlap between adjacent ultrasonic beams is maintained. With 1.5-D arrays, or by using a 1-D array and measuring the residual elevational decorrelation after correcting for the other two components, it should be possible to precisely estimate all three longitudinal components of the strain tensor in tissues using clinical array scanners. Poisson-elastograms may be important in the imaging of poroelastic, edematous and viscoelastic tissues (Konofagou and Ophir 1998).

Given the fortunate existence of significant modulus contrast in many normal and abnormal tissues, and the ability to estimate some of the components of the strain tensor, the noise performance of these estimations becomes the important parameter that dictates the achievable contrast-to noise ratio in elastograms. The Strain Filter framework has been developed to describe the tradeoffs among all the technical parameters of the ultrasound instrumentation in terms of their influence on the elastographic image parameters. Using this formalism, it has been demonstrated that axial-elastograms with high CNRe, wide strain dynamic range and good strain sensitivity can be achieved at resolutions that are on the order of the ultrasonic pulse width. These can be further improved by correcting for lateral displacements and linear axial distortions. Given further that axial or lateral elastograms display the distributions of the respective strains and not of the moduli, a contrast-transfer-efficiency (CTE) metric has been defined and calculated. This metric adds a description based on elasticity theory of the efficiency with which actual modulus contrast is converted to elastographic axial strain contrast under known conditions. We have shown that for low contrast situations such as in the normal ovine kidney, the strain image is a reasonable representation of the actual inverse modulus image. We have also shown that elastography holds promise in the evaluation of breast and prostate masses in vivo.

Many interesting challenges remain in the development of this new field. In principle, it should be possible to generate elastograms in real-time, perhaps by reducing the cross-correlation computations to 1-bit hardware operations, which have been shown to be effective, or by using fast Digital Signal Processing (DSP) chips. The ultimate limitation on speed is the speed of sound and the speed of propagation of the elastic wave in tissue (which is on the order of 1-10 m/s). The current need for a transducer holding apparatus is another major limitation. This could be overcome by increasing the frame rate of elastographic image acquisition to maintain better inter-frame coherence, by estimating the (Doyley et al. 2001), and correcting the axial-elastogram appropriately so that quality images can be generated. Another solution may involve the use of incoherent strain estimators that are less sensitive to jitter and other undesired motions. A "stress meter" in the form of an elastic layer attached to the transducer or the target may be used in conjunction with a hand-held device to allow automatic nonstationary image calibration for uneven compressions. The optimal elastographic protocols that are to be followed when imaging certain tissues are as yet unknown. These include the amount of pre-compression, the applied imaging compression, the number of sonographic frames and the (adaptive) algorithm(s) to be used for image optimization, and the relationship of these protocols to the specific elastic properties (such as contrast and nonlinear stress/strain behavior) of most tissues. While elastographic artifacts are fairly well understood, their possibly ambiguous role as detractors or facilitators of lesion detection and/or diagnosis remains unknown. Related techniques, such as high frequency, high-resolution methods applied intravascularly may also develop as useful adjuncts to the current sonographic methods. Another important area that could greatly benefit from the incorporation of elastographic techniques is the area of thermal or cryogenic tissue ablation monitoring. It is known that standard sonographic techniques are not well suited for monitoring such procedures due to their poor

contrast. We have recently shown that elastography offers high contrast and precision in monitoring laser and High Intensity Focused Ultrasound (HIFU) applications (Righetti et al. 1999). This has now been demonstrated in vivo as well from the work of Souchon et al (**Fig. 14**).

In conclusion, we believe that while elastography has progressed rapidly in the past several years, much progress has yet to be made in order for elastography to become a viable clinical and investigational tool. Even at this early stage, however, it is evident that there exists a fortunate set of favorable biological, mechanical, statistical and acoustical circumstances that, when combined, will inevitably allow the attainment of this goal.

Acknowledgement

This work was supported in-part by the National Cancer Institute (USA) Program Project Grant P 01-CA 64597 to the Ultrasonics Laboratory at the University of Texas Medical School in Houston. Subcontractors of this Program Project are Baylor College of Medicine, the University of Vermont, Thomas Jefferson University and INSERM.

References

1) Alam SK, Ophir J, Varghese T: Elastographic axial resolution criteria: An experimental study. IEEE Trans UFFC 2000; **47** (**1**): 304-309.
2) Alam SK, Ophir J, Cespedes I, et al: A deconvolution filter for improvement of time-delay estimation in elastography. IEEE Trans UFFC 1998 a; **45** (**6**): 1565-1572.
3) Alam SK, Ophir J: Reduction of signal decorrelation from mechanical compression of tissues by temporal stretching: Applications to elastography. *Ultrasound Med Biol* 1997; **23**: 95-105.
4) Alam SK, Ophir J, Konofagou E, et al: An adaptive strain estimator for Elastography. IEEE Trans UFFC 1998 b; **45**: 461-472.
5) Alam SK, Richards DW, Parker KJ: Detection of Intraocular Pressure change in the eye using sonoelastic Doppler ultrasound. *Ultrasound Med Biol* 1994; **20**: 751-758.
6) Anderson, WAD, Pathology, C.V. Mosby Co., St. Louis, 1953.
7) Bakke T: A new mechanical instrument for the measurement of fibro-elasticity with special reference to its use in the assessment of the consistency of the uterine cervix. *Acta Obstet Gynecol Scand* 1973; **52**: 277-287.
8) Brusseau E, Perrey C, Delachartre P, et al: Axial strain imaging using a local estimation of the scaling factor from RF ultrasound signals. *Ultrason Imaging* 2000; **22** (**2**): 95-107.
9) Céspedes I, Ophir J, Ponnekanti H, et al: Elastography: elasticity imaging using ultrasound with application to muscle and breast in vivo. *Ultrason Imaging* 1993; **15**: 73-88.
10) Chen EJ, Novakofski J, Jenkins WK, et al: Young's Modulus measurements of soft tissues with application to elasticity imaging. IEEE Trans UFFC 1996; **43**: 191-194.
11) D'Angelo E: Stress-strain relationships during uniform and non-uniform expansion of isolated lungs. *Respir Physiol* 1975; **23**: 87-107.
12) Demiray H: A note on the elasticity of soft biological tissues. *J Biomech* 1972; **5**: 309-311.
13) Doyley MM, Bamber JC, Fuechsel F, et al: A freehand elastographic imaging approach for clinical breast imaging: System development and performance evaluation. *Ultrasound Med Biol* 2001; **27** (**10**): 1347-1357
14) Fatemi M, Greenleaf JF: Vibro-acoustography: An imaging modality based on ultrasound-stimulated acoustic emission. *Proc Natl Acad Sci USA* 1999; **96** (**12**): 6603-8.
15) Fukaya H, Hildebrandt J, Martin C J: Stress-strain relations of tissue sheets undergoing uniform two dimensional stretch. J Appl Physiol 1969; **27**: 758-762.
16) Fung YC: Biomechanical properties of living tissues, Ch. 7, Springer Verlag, NY, 1981.
17) Galey FR: Elastic properties of fixed and fresh muscle. J Ultrastruct Res 1969; **26**: 424-441.
18) Gao L, Parker KJ, Lerner RM, et al: Imaging of the elastic properties of tissue- A review. *Ultrasound Med Biol* 1996; **22**: 959-977.
19) Garra BS, Céspedes EI, Ophir J, et al: Elastography of breast lesions: Initial clinical results. *Radiology* 1997; **202**: 79-86.
20) Harley R, James D, Miller A, et al: Phonons and the elastic moduli of collagen and muscle. *Nature* 1977; **265**: 285-287.
21) Kallel F, Ophir J, Magee K, et al: Elastographic imaging of low-contrast elastic modulus distributions in tissue. *Ultrasound Med Biol* 1998; **24**: 409-425.
22) Kallel F, Bertrand M, Ophir J: Fundamental limitations on the contrast-transfer efficiency in elastography: An analytic study. *Ultrasound Med Biol* 1996; **22**: 463-470.
23) Kallel F, Varghese T, Ophir J, et al: The nonstationary strain filter in elastography, Part II -Lateral and elevational decorrelation. *Ultrasound Med Biol* 1997; **23**: 1357-1369.
24) Kallel F, Price R E, Konofagou EE, Ophir J: Elastographic Imaging of the normal canine prostate in vitro. *Ultrason Imaging* 1999; **21**: 201-205.
25) Konofagou EE, Ophir J, Kallel F, et al: Elastographic dynamic range expansion using variable applied strains. *Ultrason Imaging* 1997; **19**: 145-166.
26) Konofagou EE, Varghese T, Ophir J, et al: Incoherent and Direct Spectral Strain Estimators in Elastography. *Ultrasound Med Biol* 1999; **25** (**7**): 1115-1129.
27) Konofagou EE, Ophir J: A new elastographic method for estimation and imaging of lateral displacements, lateral strains, corrected axial strains and Poisson's ratios in tissues. *Ultrasound Med Biol* 1998; **24**: 1183-1199.
28) Krouskop TA, Wheeler TM, Kallel F, et al: The elastic moduli of breast and prostate tissues under compression. *Ultrason Imaging* 1998; **20**: 151-159.
29) Krouskop TA, Vinson S, Goode B, et al: A pulsed Doppler ultrasonic system for making noninvasive measurements of the mechanical properties of soft tissue. *J Rehabil Res Dev* 1987; **24**: 1-8.
30) Lerner RM, Parker KJ: Sono-elasticity in ultrasonic tissue characterization and echographic imaging. Proc. 7th Eur. Comm. Workshop, J.M. Thijssen, Ed., Nijmegen, The Netherlands, 1987.
31) Lerner RM, Huang SR, Parker KJ: "Sonoelasticity" images

derived from ultrasound signals in mechanically vibrated tissues. *Ultrasound Med Biol* 1990; **16**: 231-239.

32) Lorenz A, Pesavento A, Garcia-Schurmann M, et al: New results with real time strain imaging. Frequenz 2001; **55** (**1-2**): 21-24.

33) Malinauskas M, Krouskop TA, Barry P A: Noninvasive measurement of the elastic modulus of tissue in the above-knee amputation stump. *J Rehabil Res Dev* 1989; **26**: 45-52.

34) Merritt CR, Forsberg F, Liu J, et al: In vivo elastography in animal models: feasibility studies. Abstract, American Institute of Ultrasound in Medicine, 2002 Annual Convention, Nashville TN: p. S: 98.

35) O'Donnell M, Skovoroda AR, Shapo BM, et al: Internal Displacement and Strain Imaging Using Ultrasonic Speckle Tracking. IEEE Trans UFFC 1994; **41**: 314-325.

36) Ophir J, Alam SK, Garra BS, et al: Elastography: Measurement and imaging of tissue elasticity. Proc. Instn. Mech. Engrs. Vol. 219 part H, pp. 203-233, 1999.

37) Ophir J, Cespedes EI, Ponnekanti H, et al: Elastography: a quantitative method for imaging the elasticity of biological tissues. *Ultrason Imaging* 1991; **13**: 111-134.

38) Ophir J, Cespedes I, Garra B et al: Elastography: ultrasonic imaging of tissue strain and elastic modulus in vivo. *Eur J Ultrasound* 1996; **3**: 49-70.

39) Ophir J, Kallel F, Varghese T, et al: Elastography: A systems approach, The International Journal of Imaging Systems and Technology. John Wiley & Sons, Inc, 1997; **8**: 89-103.

40) Pesavento A, Perrey C, Krueger M, et al: A time-efficient and accurate strain estimation concept for ultrasonic elastography using iterative phase zero estimation. IEEE Trans UFFC 1999; **46** (**5**): 1057-1067.

41) Ponnekanti H, Ophir J, Y Huang, et al: Fundamental mechanical limitations on the visualization of elasticity contrast in elastography. *Ultrasound Med Biol* 1995; **21**: 533-543.

42) Righetti R, Kallel F, Stafford RJ, et al: Elastographic characterization of HIFU-induced lesions in canine livers. *Ultrasound Med Biol* 1999; **25** (7): 1099-1113.

43) Righetti R, Ophir J, Ktonas, P: Axial resolution in Elastography. *Ultrasound Med Biol* 2002 a; **28** (**1**): 101-113.

44) Righetti R, Srinivasan S, Ophir J: Lateral Resolution in Elastography. Submitted to Ultras Med Biol 2002 b.

45) Rosenthal SJ, Hall TJ, Spalding C, et al: Real time palpation breast imaging. Abstract, American Institute of Ultrasound in Medicine, 2002 Annual Convention, Nashville TN: p. S: 17.

46) Saada S: Elasticity, Theory and Applications, Pergamon Press. New York 1983.

47) Sarvazyan AP, Skovoroda AR, Emelianov SY, et al: Biophysical bases of elasticity imaging. Acoustical Imaging 1995; **21**: 223-240.

48) Sarvazyan AP: Shear acoustic properties of soft biological tissues in medical diagnostics. J Acoust Soc Am Proc 125th meeting 1993; **93**: 2329.

49) Varghese T, Ophir J: An analysis of elastographic contrast-to-noise ratio performance. *Ultrasound Med Biol* 1998; **24** (**6**): 915-924.

50) Varghese T, Ophir J: The nonstationary strain filter in elastography, Part I Frequency dependent attenuation. *Ultrasound Med Biol* 1997 a; **23**: 1343-1356.

51) Varghese T, Ophir J: A theoretical framework for performance characterization of elastography: The Strain Filter. IEEE Trans UFFC 1997 b; **44**: 164-172.

52) Varghese T, Bilgen M, Ophir J; Multiresolution imaging in elastography. IEEE Trans Ultrason Ferroel Freq Cont 1998; **45**: 65-75.

53) Walker WF, Fernandez FJ, Negron LA; A method of imaging viscoelastic parameters with acoustic radiation force. *Phys Med Biol* 2000; **45** (**6**): 1437-1447.

54) Yamada H: Strength of Biological materials. Baltimore, The Williams & Wilkins, 1970.

55) Yamakoshi Y, Sato J, Sato T: Ultrasonic imaging of internal vibration of soft tissue under forced vibration. IEEE Trans UFFC 1990: **37**: 45-53.